Materials & Design 226 (2023) 111647

Contents lists available at ScienceDirect

Materials & Design

journal homepage: www.elsevier.com/locate/matdes

Achieving superior dispersion-strengthening effect in an AA5xxx Al-Mg-Mn alloy by mico-alloying

Shiwei Pan [a,b], Zidong Wang [c,*], Chunan Li [b], Di Wan [d], Xiaohua Chen [c], Kaixuan Chen [c], Yanjun Li [b,*]

[a] School of Materials Science and Engineering, Beijing Institute of Technology, 100081 Beijing, China
[b] Department of Materials Science and Engineering, Norwegian University of Science and Technology, 7491 Trondheim, Norway
[c] School of Materials Science and Engineering, University of Science and Technology Beijing, Beijing 100083, China
[d] Department of Mechanical and Industrial Engineering, Norwegian University of Science and Technology, 7491 Trondheim, Norway

HIGHLIGHTS

- A dispersion-strengthened 5xxx Al-Mg-Mn alloy was developed via micro-additions of Zr, Cr, increased Mn content and heat treatment optimization.
- Precipitation of dense Mn-rich dispersoids and Al_3Zr with an improved homogeneity across grains/dendrites is achieved, resulting in superior dispersion-strengthening effect.
- During 400 °C long-time treatment of the developed alloy, the softening from Mn-rich dispersoids coarsening is compensated by continuous precipitation of Al_3Zr.
- The as-rolled developed alloy owns an ultra-strong resistance to softening during back annealing at elevated temperatures, as high as 550 °C.

GRAPHICAL ABSTRACT

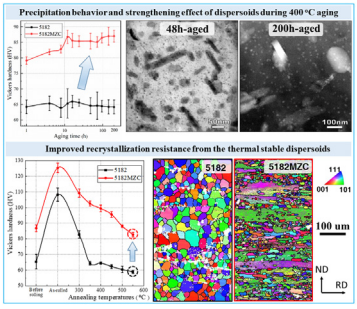

ARTICLE INFO

Article history:
Received 30 November 2022
Revised 14 January 2023
Accepted 19 January 2023
Available online 21 January 2023

Keywords:
Al alloys
Mn-rich dispersoid
Al_3Zr
Precipitation
Dispersion-strengthening
Mechanical properties

ABSTRACT

5xxx Al-Mg based alloys are widely applied as non-heat-treatable alloys. In this work, we designed a dispersion-strengthening Al-4Mg-1Mn-0.3Fe-0.2Si-0.2Zr-0.2Cr (wt.%) alloy. By applying ramp heating and 400 °C isothermal aging, a significant dispersion-strengthening effect through the formation of various types of dispersoids was achieved. Detailed scanning electron microscopy (SEM) and transmission electron microscopy (TEM) analysis revealed the precipitation behaviors of nanoscale Mn-rich dispersoids and Al_3Zr nanoparticles during heat treatments. As a result, an increment of 48 MPa in yield strength was obtained compared with the reference 5182 alloy. Meanwhile, the modified alloy shows a good heat resistance at 400 °C with little loss of yield strength until 200 h of heating. This has been attributed to the further precipitation of Al_3Zr particles which counteracts the coarsening of Mn-rich dispersoids. Moreover, the addition of peritectic element Cr was found to significantly promote the precipitation of Al_6(Mn,Fe,Cr) in dendritic center regions, thus improving their global distribution across dendrite arms. The presence of dense dispersoids can also improve the recrystallization resistance of the deformed alloy during annealing, thus retaining the deformation fiber structure and significantly

* Corresponding authors.
E-mail addresses: wangzd@mater.ustb.edu.cn (Z. Wang), yanjun.li@ntnu.no (Y. Li).

https://doi.org/10.1016/j.matdes.2023.111647

retarding the recrystallization behavior. This research demonstrates an effective strategy to develop high-performance 5xxx series alloys strengthened via dispersoids.

1. Introduction

5xxx series Al-Mg based alloys are widely used in automobile and ship manufacturing industries due to their good combination of strength, ductility, weldability and formability [1]. As a typical kind of non-heat-treatable alloys, 5xxx alloys achieve high strength through strong solution-strengthening and work-hardening effects of Mg solute atoms, which has a relatively high solid solubility in Al matrix [2]. With a given amount of deformation, higher Mg concentrations increase the strain hardening response, obtaining more retained strain in the as-deformed alloy, thus improving the strength [3]. However, Mg contents in most commercial 5xxx alloys usually fall within the range of 3–6 wt% [2,4-6] This is because higher Mg contents will induce serious formation of β-Al_3Mg_2 phase along grain boundaries, resulting in edge-cracking and stress corrosion cracking. Taking this factor into consideration, additions of other elements in Al-Mg based alloys for the purpose of further improving the strength is necessary, which are expected to provide additional strengthening effect but not chemically interacting with Mg and consuming it from the solid-solution.

Dispersion-strengthening, by precipitating nano-sized dispersoids in Al matrix, has drawn considerable attentions to improve the mechanical strength of Al alloys during the past several decades [7-9]. Unlike age hardening precipitates, the dispersoids are relatively thermal-stable at elevated temperatures, thus can provide additional strength contribution by increasing the recrystallization resistance and reserving the deformed fiber structures during back annealing [10,11]. This characteristic enables dispersion-strengthening with great potential to be applied in non-age-hardened wrought Al alloys, for example 3xxx and 5xxx alloys. Generally, the typical dispersoids-forming elements include some transition elements like Ti, Zr, Hf, Mn, Cr, etc, and several rare-earth elements such as Sc, Yb, Er [12-18]. Particularly, the relatively inexpensive Zr and Mn are the most widely used options in industrial production [19].

Many commercial Al-Mg-Mn 5xxx alloys in practical applications contain relatively high Mn contents, such as AA5454 (Al3Mg0.8Mn), AA5083 (Al4.5 Mg0.7Mn), AA5754 (Al3Mg0.3Mn) and AA5182 (Al4.5 Mg0.4Mn) [20,21], while Fe and Si as ever-present impurities are inevitably detected. Accordingly, several kinds of Fe and Mn-bearing compounds can form both as coarse constituent phases during solidification and as fine dispersoids during homogenization or hot rolling. It was reported that equilibrium Al_6(Mn,Fe) with orthorhombic structure precipitated as the main dispersoids in AA5182 alloy after homogenization treatment [22]. More specifically, two different morphologies (rhomboidal and plate-like) of Al_6(Mn,Fe) dispersoids with various sizes can be observed [23], which was supposed to be controlled by the homogenization parameters [24]. Besides, the research work of Li et al. [9] and Engler et al. [21,25] proved that both α-$Al_{12}(Mn,Fe)_3Si_{1-2}$ with cubic structure (Pm3) and Al_6(Mn,Fe) dispersoids could precipitate during homogenization in several Al-Mg-Mn alloys, while the type of dispersoids is highly governed by combined Si and Mg contents. However, these dispersoids are mainly used to modify the grain structure instead of acting as strengthening phases in 5xxx alloys, since conventional homogenization at temperatures above 500 °C usually leads to large sizes and small number densities of dispersoids. Recently, it was found that heat treatment at relatively lower temperatures (275–425 °C) resulted in the formation of nano-sized Al_6Mn- and Al_4Mn-type dispersoids (containing Fe and Cr) with finer size in an industrial Al-5 %Mg-0.8 %Mn alloy [7], providing a significant strengthening effect. Nonetheless, the difficulty in obtaining large volume fractions of uniformly distributed fine dispersoids is still a challenge for Al-Mg-Mn alloys because of the limited solubility and strong segregation tendency of Mn solute atoms.

Zr, as an economical $L1_2$ dispersoid-forming element, is well known to produce Al_3Zr nanoparticles coherent to the matrix in various Al alloys [17,26]. It was shown that an addition of 0.25 wt% Zr provided obvious hardness increment (∼12HV) after annealing in a binary Al-Mg alloy [27]. A recent study [28] showed that an addition of 0.25 wt%Zr in a model alloy Al-3 Mg-1.1Mn could increase the hardness of the as-cast alloy from 63 HV to ∼ 80 HV through two-steps (350 °C + 400 °C) aging treatments. In this case, plate-like Al_6Mn, nano-sized Al_3Zr and icosahedral quasi-crystalline I-phase were formed in the Al matrix. It was suggested by the authors that the dense I-dispersoid was metastable and only enriched with Mn because this alloy was almost free of Si and Fe. However, the precipitation sequence could be totally different in commercial Al alloys with inevitable presence of Fe and Si elements. In our previous study [29], α-Al(Mn,Fe)Si was identified as the dominant Mn-bearing dispersoid in Al-Mn-Fe-Si-Zr system, and the precipitation kinetics of Al_3Zr was also promoted by Si solute atoms. Also, Zr exhibits opposite segregation behavior during solidification compared with Mn, which implies precipitation of dense Al_3Zr could occur in Mn-depletion zones. From this aspect, the introduction of Al_3Zr dispersoids into Al-Mg-Mn series alloys by Zr-microalloying is anticipated to further improve dispersion-hardening effect. In general, the types, compositions, size, densities and precipitation behaviors of dispersoids in commercial Al-Mg-Mn alloys containing Zr and Cr could be complex and the corresponding dispersion-strengthening effects need to be assessed. To the authors' best knowledge, limited information in literatures can be found.

In the present study, an Al-4 Mg-1Mn-0.3Fe-0.2Si-0.2Zr-0.2Cr was designed and prepared by further increasing Mn content in a commercial AA5182 alloys to 1 wt% and alloying by a small amount of Zr and Cr. Herein, the addition of Cr is expected to improve the stability of Mn-bearing dipsersoids based on our previous finding [30]. These alloys own higher Mn content and extra Zr content in comparison to AA5083. The design strategy of this alloy is to achieve high density Al_3Zr and Mn-rich dispersoids after aging. This study aims at: (1) revealing the precipitation sequence and nucleation mechanisms of various dispersoids subjected to different aging regimes; (2) investigating the evolution of dispersoids and their dispersion-strengthening effect during 400 °C isothermal aging; (3) studying the effect of dispersoids on retarding the recrystallization of as-deformed alloy during back annealing.

2. Materials and methods

An experimental Al-4Mg-1Mn-0.3Fe-0.2Si-0.2Zr-0.2Cr (wt.%) alloy, denoted as 5182MZC, was prepared by conventional casting. Actually, the compositions of this alloy are closer to AA5083 alloy, in terms of Mn and Cr contents. However, in order to quantify the influences of the dispersoid-forming elements on the precipitation behavior of dispersoids and corresponding dispersion hardening

efficiency, a DC-cast AA5182 billet (refined by Al-Ti-B) supplied by Hydro Inc. was utilized as a raw material and also used as the reference alloy. After re-melting in an induction furnace, Al-10wt.% Mn, Al-8wt.%Zr and Al-10wt.%Cr master alloys were added at 780 °C, holding for 1 h with regular stirring to ensure adequate dissolution. Then, the degassed liquid melt was cast into a preheated copper mold to obtain an ingot with a dimension of 30 × 70 × 100 mm^3. In addition, a binary Al-0.24wt.%Zr alloy was also cast as reference alloy. Chemical compositions of all as-cast alloys identified by X-ray Fluorescence Spectrometer (XRF) are listed in Table 1. In comparison to AA5182 alloy, the content of Mn in the modified alloy was increased to 1 wt%, while a loss of about 0.6 wt% Mg caused by re-melting was identified.

Two different heat-treatment methods were conducted in the present study. Firstly, ramp-heating was applied on the as-cast samples from 25 °C up to 600 °C with a rate of 50 °C /h. During this process, 10 samples were water-quenched one after another at various temperatures in order to study the precipitation sequence. Secondly, 400 °C isothermal aging up to 200 h was carried out on samples as-heated to this temperature by ramp heating, which was used to evaluate the heat resistance of 5182MZC alloy. Particularly, ingots after isothermal aging at 400 °C for 48 h were chosen and sliced with a thickness of 20 mm, then cold rolled at room temperature to 5 mm-thick plates with a reduction of 75 %. After that, the cold-rolled samples were subsequently isochronal annealed for 1 h at various temperatures from 300 °C to 550 °C, respectively.

Vickers microhardness of heat-treated samples were measured under 1 kg load for 10 s dwell time, and at least eight indentations were made for each sample. Dog-bone shaped tensile specimens with gauge length of 30 mm and cross section of 2 × 6 mm^2 were prepared according to ASTM-E21-09 standards [31] and uniaxial tensile testing was performed at ambient temperature with a constant displacement rate corresponding to an initial nominal strain rate of 1 × 10^{-3} s^{-1}. Tests for each condition were repeated for three times to ensure the reproducibility.

The as-cast microstructure was characterized by a *Zeiss Ultra* field-emission SEM equipped with energy dispersive spectroscopy (EDS) and electron backscatter diffraction (EBSD), while back-scattered electron (BSE) mode was used to investigate the distribution of dispersoids throughout the dendrite. Foils for TEM observation were thinned by twin-jet electropolishing in an electrolyte of 33 % nitric acid in methanol at −20 °C. *FEI TecnaiF30* and *Talos F200X G2* TEMs equipped with EDS were operated at 200 kV for bright/dark field imaging, selected area diffraction pattern (SADP), and high angle annual dark field (HAADF) imaging as well as EDS mapping for compositional analysis. The mean sizes of Al_3Zr and Mn-rich dispersoids were determined based on > 200 particles from TEM results by using *Nano Measurer 1.2*.

3. Results

3.1. As-cast microstructure

Fig. 1a and b present the grain structures of as-cast 5182 and 5182MZC alloys. Grain boundaries with misorientation angles>15° are identified and labeled with black lines in EBSD maps. Obviously, in both alloys, solidification grains show globular shape, reflecting the formation of equiaxed dendritic structure during solidification. It appears that the average grain size of 5182MZC (152 μm) is larger than the reference 5182 alloy (125 μm). This discrepancy can be ascribed to the Zr-poisoning effect on the grain refiner TiB_2 particles in the modified alloy with Zr addition referring to a previous report [32]. Fig. 1c is a SEM micrograph with the corresponding EDS mapping results, showing several different constituent phases in as-cast 5182MZC alloy. It can be found Al_6(-Mn,Fe,Cr) with skeletal morphology and bright contrast is the dominant constituent phase, which mainly distributes within inter-dendritic regions and along grain boundaries. This is a common Mn/Fe-containing primary particle in 5xxx alloys and was reported to appear as temperature cools down to ~ 620 °C during solidification [20]. It is different from the reference AA5182 alloy, in which Al_mFe and Al_3Fe are the major constituent particles [22]. This is due to the high content of Mn in 5182MZC alloy. Also, it is worth of noting that a slight Zr enrichment can be found in Al_6(Mn,Fe,Cr) constituent phase, implying that Zr can partially substitute Fe and Mn content in the constituent particle, which needs a further investigation in the future. Similar to the observations in [20,21], another major constituent particle presented in Fig. 1c could be identified as Mg_2Si phase with dark contrast (Fig. 1c), although the poor resolution of the SEM-EDS detector failed to identify the Kα-Si signals in Fig. 1d. It has to be mentioned that the Si-rich α-$Al_{15}(Mn,Fe)_3Si_2$ is rarely detected here because of the high Mg/Si ratio in the present alloy, which is different from the observation in ref [7]. In addition, a minor fraction of ε-$Al_{18}(Mn,Cr)_2Mg_3$ and Al_3Zr particles are also observed within dendrite arms.

3.2. Ramp heating from RT to 600 °C

3.2.1. Evolution of microhardness

Fig. 2 presents the evolution of Vickers hardness (HV) of the studied alloys during ramp heating from RT to 600 °C. Although with a slightly lower Mg content, the as-cast 5182MZC exhibits a higher hardness value of 74.9 HV than that of 5182 alloy. This is because that the Mn and Cr solute atoms existing in the matrix can provide considerable contributions to the hardness of the modified alloy. During ramp heating, 5182MZC alloy also displays a more obvious age-hardening response with the highest peak value among three experimental alloys. More specifically, a quick rise of hardness of 5182MZC alloy starts between 200 and 250 °C and reaches a value of 77 HV, then in the range of 250–450 °C the hardness slowly increases to 79.2 HV. Above 450 °C, there is another increase in hardness until reaching the peak value of 84 HV at 550 °C. After that, further heating to higher temperature induces decrease in hardness, which may be associated with the coarsening and dissolution of the strengthening phases. In comparison, no obvious age-hardening behavior could be observed in the reference 5182 alloy especially in the range of 300–600 °C since its Mn content (0.2 wt%) is insufficient to generate significant precipitation of dispersoids. For Al-Zr alloy, it displays a slow precipitation kinetics and obtains the maximum hardness increment of 4 HV until heating to 550 °C. Therefore, the total hardness growth of 9.2 HV obtained in 5182MZC is ascribed not only to the precipitation of

Table 1
Chemical compositions of the as-cast alloys (wt. %).

Alloy	Al	Mg	Mn	Fe	Si	Zr	Cr	Ti
5182	Bal	4.12	0.22	0.36	0.19	–	–	0.02
5182MZC	Bal	3.65	1.02	0.34	0.24	0.22	0.19	0.01
Al-Zr	Bal	–	–	<0.01	<0.01	0.24	–	–

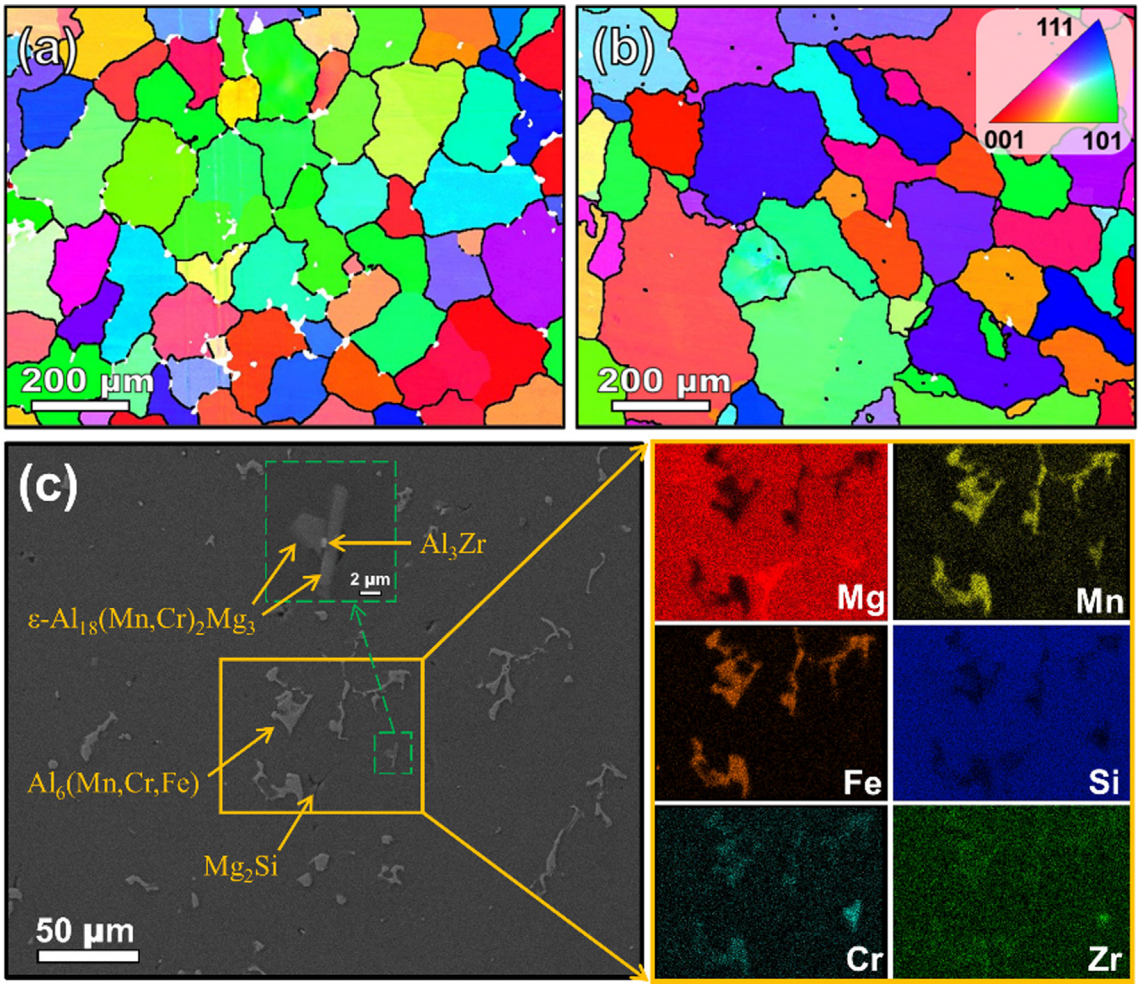

Fig. 1. EBSD maps of the as-cast (a) 5182 and (b) 5182MZC alloys showing the grain structure; (c) SEM micrograph of the as-cast 5182MZC alloy, and insets on the right side are EDS mapping results of the rectangle area in (c) showing Mg_2Si, $Al_6(Mn,Fe,Cr)$, ε-$Al_{18}(Mn,Cr)_2Mg_3$ and Al_3Zr constituent phases formed during solidification. Note detailed composition of each phase was identified by EDS point scanning but not shown here.

Al_3Zr particles, but also to the precipitation of Mn- and Cr- containing phases.

3.2.2. Precipitation of various phases

Precipitation of various phases in 5182MZC at 400, 500 and 550 °C during ramp heating was characterized by TEM, and representative micrographs as well as EDS point analysis results are displayed in Fig. 3. After ramp-heating to 400 °C, myriads of fine dispersoids with the average diameter of 19.2 nm have precipitated from the Al matrix (Fig. 3a and b), which are identified as α-Al(Mn,Fe)Si phase by the FFT diffraction pattern [9]. The partitioning of Cr into α-dispersoids does not supposed to occur at this temperature mainly because of its low diffusivity. It is also found the distribution of the α-dispersoids is quite inhomogeneous, as reflected by the significant difference in densities between Fig. 3a and c. Apart from dispersoids, several coarse particles with sizes of a few hundred nanometers can be observed, as seen in Fig. 3c. EDS analysis (point 1) as well as SADP (inset in Fig. 3c) of the same particle confirm that the phase with shallow contrast is equilibrium β-Al_3Mg_2 with FCC structure, which is the same as that shown in Ref. [6]. In addition, a few coarse Mg_2Si particles with dark contrast can also be observed (see point 2). After heating to 500 °C (see Fig. 3d-f), the Mn-rich dispersoids grow to the size of dozens of nanometers and appear with either blocky or platelet-like shapes. SADP along [1 1 0] zone axis of Al matrix shown in the inset confirm the presence of the observed dispersoids. In addition to a few α-Al(Mn,Fe)Si, EDS analysis reveals that a large fraction of the dispersoids, independent of their morphologies, are $Al_6(Mn,Fe,Cr)$ with high Mn content and trace level of Cr and Fe contents (point 3). This is a common phase frequently observed in homogenized 5xxx series alloys such as 5083 [20] and 5182 [22]. Meanwhile, spherical Al_3Zr nanoparticles also precipitate from the matrix at this state, which own typical $L1_2$ structure as revealed by the HRTEM examination (see inset in Fig. 3e). The distribution of Al_3Zr is also inhomogeneous, but exhibits an opposite trend to Mn-rich dispersoids (see Fig. 3e and f). With further increasing temperature to 550 °C, obvious coarsening of all Mn-rich dispersoids happens with the reduction in density, as seen in Fig. 3g and h. At the same time, the growth of Al_3Zr is evident. However, it is worth noting that the number density of Al_3Zr dispersoids obtained in the present alloy is lower, while the distribution is less homogeneous than that of binary Al-Zr reference alloy (Fig. 3h and i).

To our surprise, careful TEM examination shows that a large number of plate-shaped Al_3Zr phase with larger size have also formed in the alloy. Fig. 4a shows a typical HRTEM image of such Al_3Zr taken along the $\langle 0\,0\,1\rangle_{Al}$ zone axis. As can be seen, some thick lath-shaped phase (length: 5–15 nm, width: 3–5 nm) is attached onto one Mn-rich dispersoid. Fast Fourier Transform (FFT, see Fig. 4b) clearly shows the presence of super-lattice spots as indicated by the yellow circles, confirming the $L1_2$ structure. As

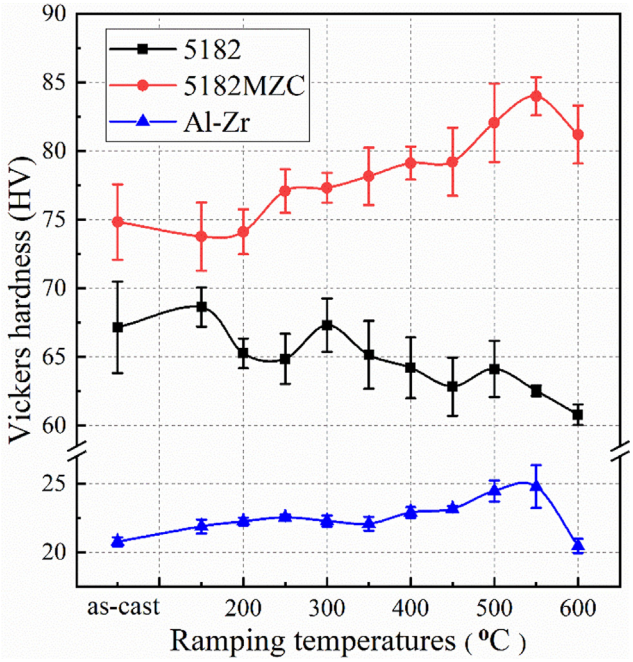

Fig. 2. Evolution of Vickers microhardness as a function of temperatures during ramp heating with a heating rate of 50 °C/h for 5182, 5182MZC and Al-Zr alloys.

revealed by the Inverse Fast Fourier Transform (IFFT, see Fig. 4c) using these super-lattice reflections, the $L1_2$-structured ordering phase appears at the same location of the lath-like phase in Fig. 4a. In this case, this lath-like phase can be identified as Al_3Zr and its precipitation around Mn-rich dispersoids can be explained by the heterogeneous nucleation of Al_3Zr on the pre-formed Mn-rich dispersoid during ramp heating, which is similar to our previous study in a 3xxx alloy [29]. As a result, the content of solute Zr atoms available for homogeneously nucleation in Al matrix is thereby reduced, thus causing a lower density of spherical Al_3Zr dispersoids as shown in Fig. 3h.

3.3. Isothermal aging after ramp heating to 400 °C

3.3.1. Evolution of microhardness

Hardness evolution of 5182 and 5182MZC alloys during a long-time isothermal aging at 400 °C up to 200 h is presented in Fig. 5. It can be found that the hardness of 5182MZC gradually increases with aging time and reaches a peak value of 86.7 HV after 12 h aging. Compared with its as-cast state, a considerable hardness increment of 11.8 HV is obtained, reflecting the further precipitation of strengthening dispersoids. With further increasing aging time, the hardness slightly decreases to 85.4 HV after 48 h aging at first, then rebounds to 87 HV until 200 h. Therefore, it proves that 5182MZC also exhibits high heat resistance at 400 °C. In contrast, 5182 alloy shows no obvious precipitation hardening during isothermal aging. After 200 h, a microhardness of 64.2 HV is achieved, which is even lower than that (67.1 HV) of the as-cast state.

3.3.2. Evolution of dispersoids

TEM images of 5182MZC alloy after 400 °C isothermal aging for 12 h, 48 h and 200 h are displayed in Fig. 6, and the corresponding statistical size distribution results of both Mn-rich dispersoids and Al_3Zr are shown in Fig. 7. After 12 h aging, dense Mn-rich dispersoids can be observed but the distribution is very inhomogeneous. In dendrite center region a lot of cuboid dispersoids with the size smaller than 50 nm are detected, while coarser lath-like dispersoids with lower density dominate at dendrite periphery regions. Corresponding size distribution in Fig. 7a reveals that the average equivalent diameter of these Mn-rich dispersoids is 36.9 nm. EDS mapping (see Fig. 8) further reveals that most Mn-rich dispersoids here are Al_6(Mn,Fe,Cr). It has to be mentioned that a small amount of α-Al(Mn,Fe,Cr)Si, reflected by its characteristic diffraction motif (inset in Fig. 6a) [33], are also present. Meanwhile, some rhomboidal β-Mg_2Si phase with dark contrast can also be occasionally observed in HAADF-STEM mode such as the one in Fig. 8. It is interesting to see several Al_6(Mn,Fe,Cr) dispersoids are attached to onto surface of β-Mg_2Si. As shown in Fig. 6d and Fig. 7b, only a small number of Al_3Zr with a mean radius of 2.1 nm can be found in the sample, showing the precipitation of Al_3Zr dispersoids is limited in this stage. Therefore, the super-lattice spots from Al_3Zr in SADP (inset in Fig. 6a) is very faint because of the extremely low density.

In the sample after 48 h aging, the distribution and morphology of Mn-rich dispersoids barely changes compared with the 12 h-aged sample. It is found from Fig. 7a that their equivalent diameter slightly decreases to 35.2 nm, which may be explained by the poor statistical from TEM images since the distribution of Mn-rich dispersoids are rather inhomogeneous. Besides, at this stage, an increased density as well as a smaller inter-particle spacing of Al_3Zr nanoparticles are distinctly observed (Fig. 6e), which can also be reflected by the sharp super-lattice spots from the inset in Fig. 6b. Statistical result of Al_3Zr dispersoids only shows a small radius increment from 2.1 to 2.4 nm with a narrow size distribution (Fig. 7b), thus indicating further precipitation of Al_3Zr from the matrix.

After long time aging up to 200 h, Mn-rich dispersoids show an obvious coarsening with an increase in size to 65.3 nm (Fig. 7a). In this case, the density of Mn-rich dispersoids decreases throughout the dendrite arms, of which the fraction of lath-like dispersoids seem to rise, as shown in Fig. 6c. Similarly, there is a dramatic increase in mean radius of Al_3Zr to 5.2 nm at this state (Fig. 7b). The distribution of dense spherical Al_3Zr nanoparticles shown in Fig. 6f in comparison to Fig. 6e indicates only a small reduction in number density compared with the 48 h-aged sample. This illustrates that Al_3Zr is more resistant to coarsening than Mn-rich dispersoids during aging time from 48 to 200 h. During this period, a slow coarsening of Al_3Zr coexists with a significant coarsening of Mn-rich dispersoids, which determines the final microstructure in Fig. 6c and f.

To evaluate the microstructural thermal stability of 5182MZC alloy at 400 °C, SEM-BSE micrographs of the 200 h-aged sample were taken in order to reveal the overall distribution of dispersoids within the dendrite structure. The sample was well polished to 0.5 μm and then electro-polished in electrolyte of 33 % nitric acid in methanol at −30 °C and 20 V for 45 s. In Fig. 9a, two dendrite arms can be distinguished within a grain, while coarse Al_6(Mn,Fe,Cr) constituent particles with bright contrast are distributed along the grain boundary and in the inter-dendritic regions. As can be seen, a high density of cuboid and lath-like Mn-rich dispersoids can still be observed throughout the dendrite arms even after 200 h long-time aging. Enlarged images in Fig. 9b and c demonstrate their size gradually increases from dendrite center towards the periphery while the density shows an opposite trend, which is consistent with the TEM images shown in Fig. 6. Similarly, Al_3Zr nanoparticles also exhibit inhomogeneity of distribution and the dense Al_3Zr zone (see Fig. 9c) is located at the dendrite center, the same as the Mn-rich dispersoids. It is worth of noting that this phenomenon seems abnormal since Mn (eutectic element) and Zr (peritectic element) show the opposite segregation tendency during solidification [29], which could be related to the addition of Cr (as discussed in Section 4.2). Besides, only a narrow dispersoid-free zones can be detected in inter-dendritic regions

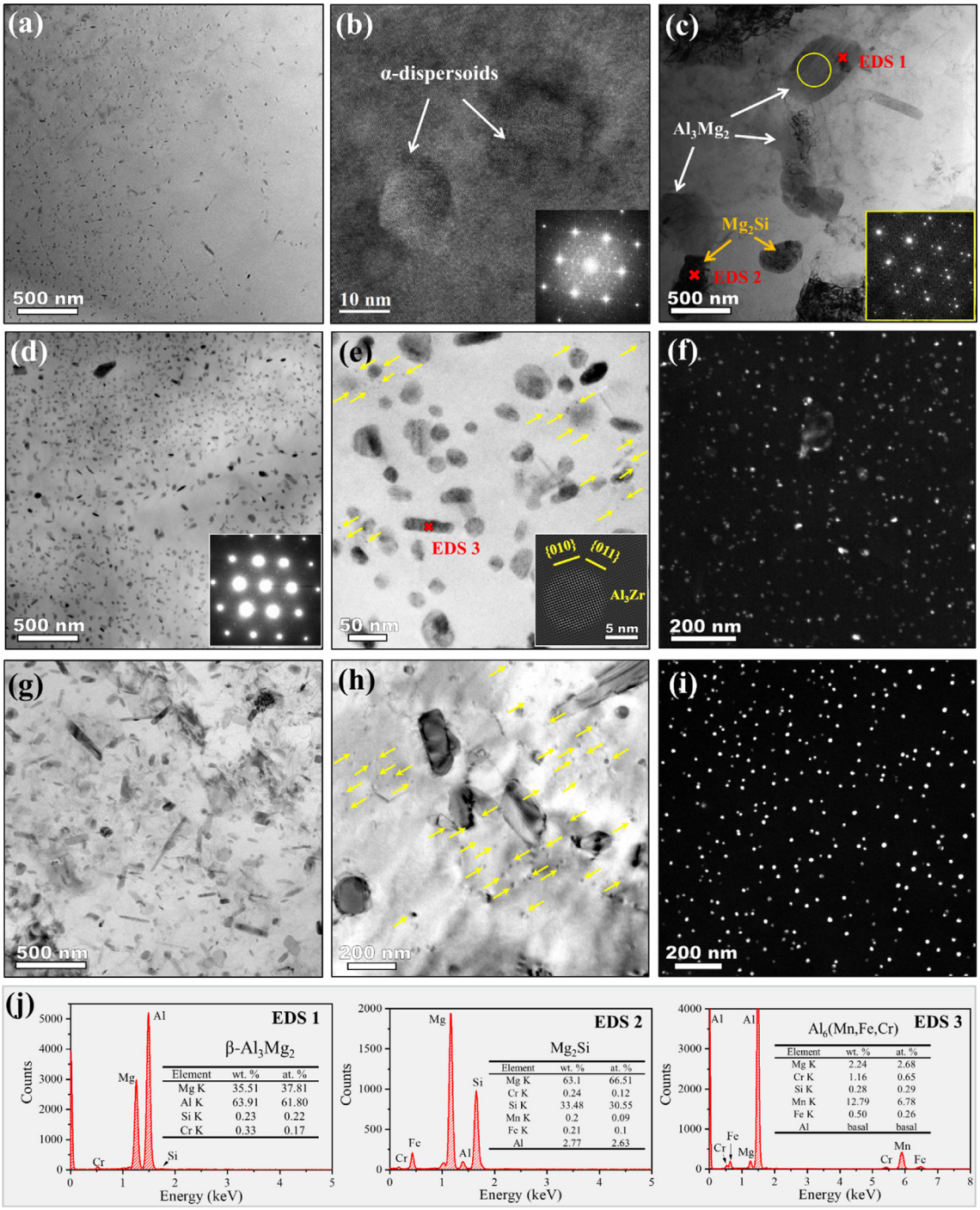

Fig. 3. TEM micrographs of the 5182MZC alloy as-heated to (a-c) 400 °C; (d-f) 500 °C; (g, h) 550 °C. (a) At 400 °C, dense dispersoids precipitate from the Al matrix with very fine size and inhomogeneous distribution. High resolution image together with it FFT in (b) reveals the structure of the α-dispersoid. In addition, some Mg_2Si and sub-micron Al_3Mg_2 phase are also observed at 400 °C and inset in (c) shows SADP of Al_3Mg_2. At 500 °C, the Mn-rich dispersoids grow, while very fine Al_3Zr starts to precipitated with various densities at different areas, as indicated by yellow arrows in (e) and dark-field image in (f). The inset in (e) shows the $L1_2$ structure of Al_3Zr. All the dispersoids grows and coarsens after heating to 550 °C as seen in (g, h). EDS point scanning were used to identify the composition of various phases during ramp-heating and corresponding spectrums are displayed in (j). Besides, dark-field image of binary Al-Zr alloy as-heated to 550 °C is shown in (i) here for reference. (For interpretation of the references to color in this figure legend, the reader is referred to the web version of this article.)

(see Fig. 9a), indicating that the dispersoids have a strong resistance to dissolution. In general, 5182MZC alloy shows a good thermal stability with dense dispersoids after 200 h aging at 400 °C, which are supposed to provide considerable dispersion-strengthening effect.

3.3.3. Tensile properties

Tensile stress-strain curves of 5182MZC and 5182 alloys after different heat treatments are presented in Fig. 10. The yield strength, ultimate strength and elongation derived from tensile curves are displayed in Table 2. As can be clearly seen, upon aging

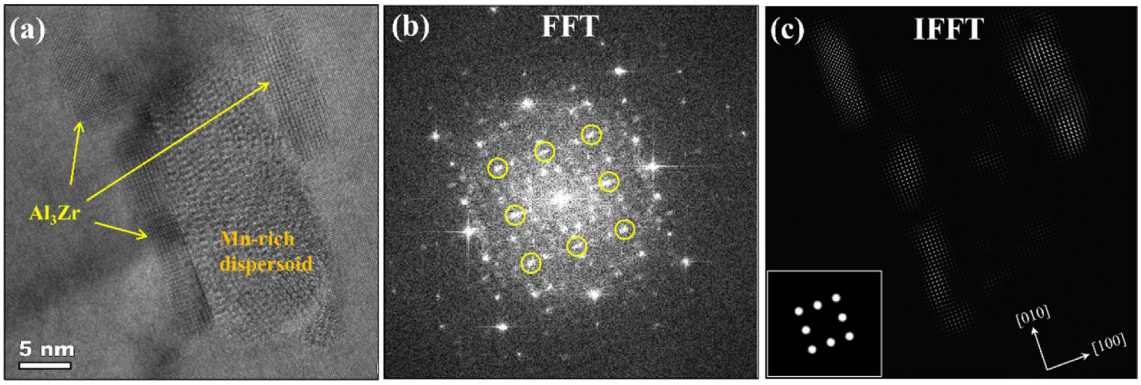

Fig. 4. TEM images of 5182MZC alloy after ramp-heated to 550 °C. (a) HRTEM image shows heterogeneous nucleation of Al_3Zr with abnormal morphology on Mn-rich dispersoid; (b) FFT pattern of (a) and the superlattice spots are marked by yellow circles; IFFT of the superlattice spots in (b) showing the abnormal Al_3Zr with $L1_2$ structure. (For interpretation of the references to color in this figure legend, the reader is referred to the web version of this article.)

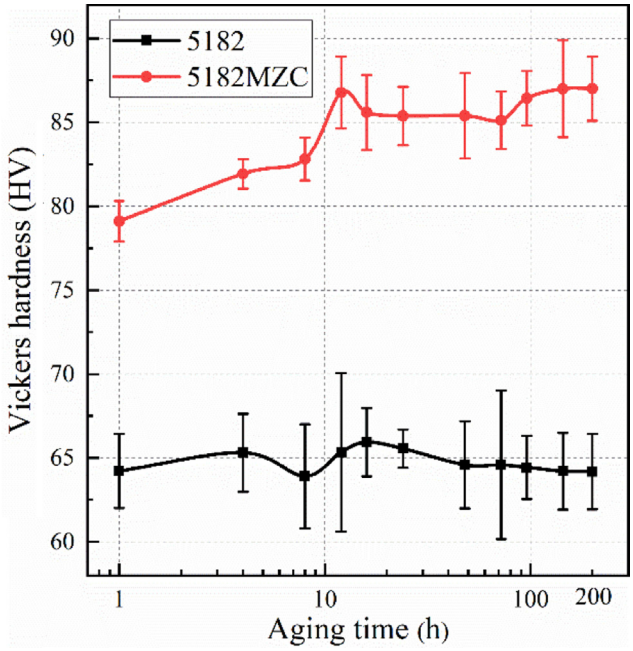

Fig. 5. Temporal evolution of the Vickers microhardness of 5182 and 5182MZC alloys during isothermal aging at 400 °C after ramp heating to this temperature. To minimize the systematic error, all the data for each alloy were collected on the same sample with various aging time.

at 400 °C for 12 h, 5182MZC alloy obtains a significantly improved yield strength of 135 MPa, which is corresponding to an increment of 23 MPa (21 %) compared with the as-cast state. Based on TEM observations, this increment is mainly attributed to the dispersion-strengthening effect from precipitated dispersoids. After longer time aging, 5182MZC exhibits relatively stable yield strengths of 135 MPa at 48 h and 134 MPa at 200 h, which are consistent with the microhardness results in Fig. 5. It illustrates that 5182MZC owns an outstanding heat resistance during 400 °C long time exposure. In contrast, 5182 alloy, with a low content of Mn, shows a negligible dispersion-hardening effect and much lower yield strength. During isothermal aging, a stable yield strength of only ~ 90 MPa is obtained without obvious variation. Besides, it should be mentioned that both alloys here exhibit poor elongation values of < 6 %. This is probably associated with the presence of coarse constituent phases at grain boundaries formed during solidification, which may induce cracks initiation because of stress concentration. Even so, much higher ultimate strengths can still be obtained in all 400 °C aged 5182MZC alloy, while the strength increment after yield point are also higher than that of the 5182 alloy at each state. This demonstrates an improved work hardening ability of 5182MZC.

3.4. Recrystallization resistance

To study the influences of the dense dispersoids on the recrystallization behavior of the cold-rolled alloys in the state, 75 % cold rolling was conducted on both 5182 and 5182MZC alloys after 400 °C/48 h aging treatments. Fig. 11a demonstrates the hardness evolution of the cold-rolled 5182 and 5182MZC alloys as a function of annealing time during isothermal annealing at 400 °C, while Fig. 11b shows the hardness after 1 h isochronal annealing at different temperatures. Evidently, both alloys achieve considerable work hardening after rolling, reaching 108 HV and 126 HV, respectively. During 400 °C annealing (Fig. 11a), a quick drop in hardness of 5182 can be observed after 1 h, reaching to 64.3 HV which is almost back to the value of 65 HV before rolling. This indicates that 5182 cannot resist recrystallization at this temperature. On the contrary, the hardness of 5182MZC first decreases to 99.6 HV after 1 h and then slowly decreases to 94 HV until 24 h, showing a strong resistance to softening at 400 °C. During annealing at different temperatures (Fig. 11b), the hardness of 5182 sample drastically decreases to 82 HV at 300 °C and then further decrease to 64 HV at 350 °C, which is very close to the value before rolling, indicating a fully recrystallization has happened. With further increasing annealing temperatures, the hardness slightly fluctuates and finally tends to stabilization. In comparison, 5182MZC alloy exhibits a much slower decreasing rate of hardness with increasing annealing temperatures. More specifically, after 1 h annealing at 450 °C, the 5182MZC sample still owns a relatively high hardness values of 96 HV, which should be attributed to the extended recovery process. Only after 500 °C/1h annealing, the hardness of the deformed alloy decreases to the level of as-aged state, indicating a superior resistance to softening in comparison with 5182 samples.

To further reveal the effect of dispersoids on recrystallization behavior, EBSD characterization was conducted on both alloys after annealing at 550 °C for 1 h. As seen in Fig. 11b, the annealed 5182 alloy is fully recrystallized with an average grain size of ~ 21 μm. In contrast, as shown in Fig. 11c, only partial recrystallizaiton has been achieved in 5182MZC alloy, where a large fraction of deformation structure is retained. Both the deformed grains (elongated along the RD) with high density dislocations and the newly formed recrystallized grains (mostly finer than 10 μm) coexist in annealed 5182MZC sample, which can be distin-

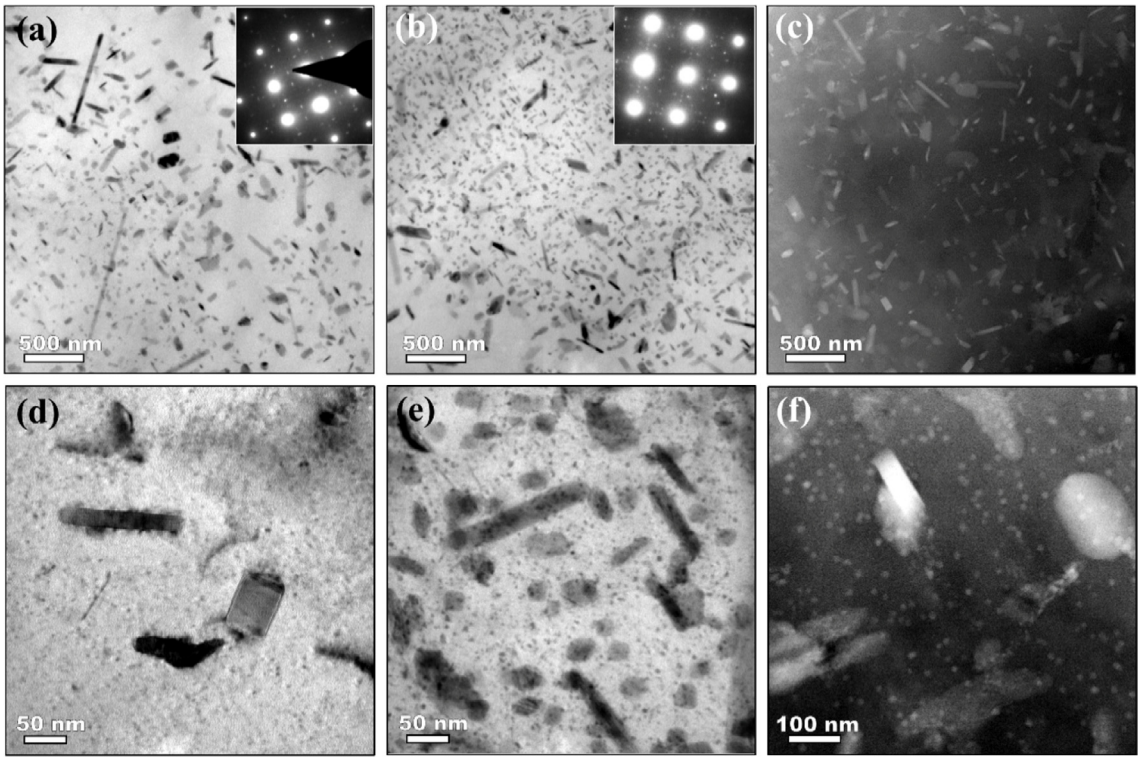

Fig. 6. TEM images of the 5182MZC alloy after isothermal aging at 400 °C for (a,d) 12 h, (b,e) 48 h and (c,f) 200 h, respectively. (a-b) bright-field (BF) micrographs and (c) HAADF-STEM image are taken from the transition areas from dendrite periphery to center showing the size, density and distribution of Mn-rich dispersoids, while BF images (d, e) plus HAADF-STEM image (f) are taken at high magnifications in order to reveal the evolution of Al_3Zr nanoparticles. Insets in (a, b) are corresponding SADP along [001] zone axis of the matrix, showing the appearance of super-lattice spots from Al_3Zr.

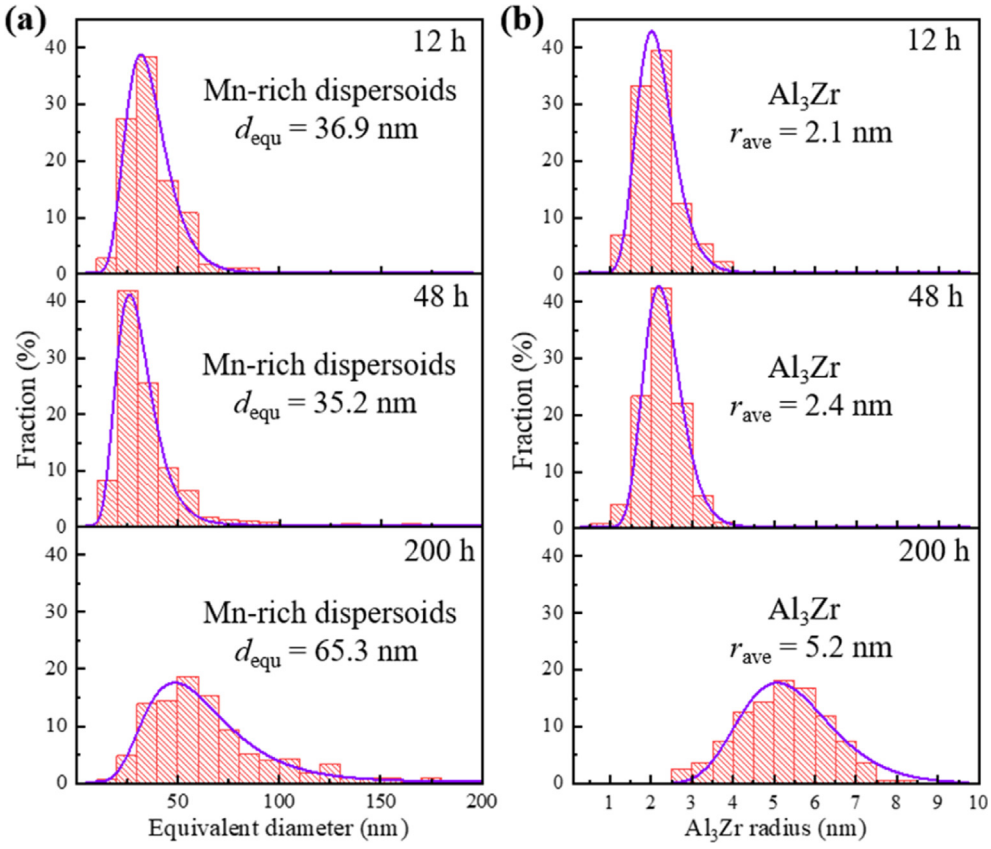

Fig. 7. Respective size distribution histograms of the (a) Mn-rich dispersoids and (b) Al_3Zr nanoparticles of the 5182MZC alloy after aging at 400 °C for various time.

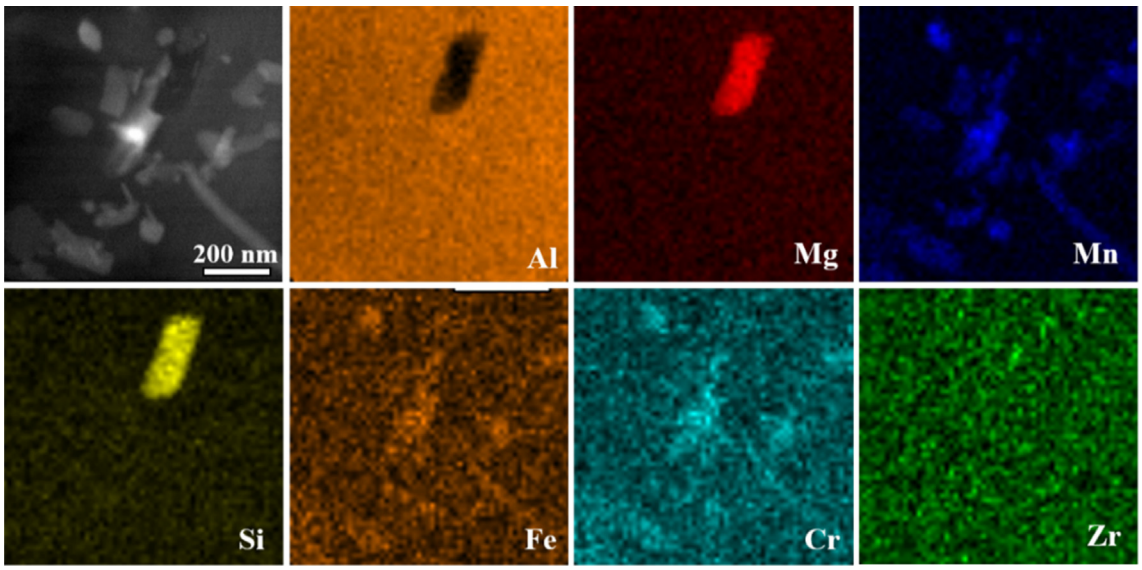

Fig. 8. HAADF-STEM image and corresponding EDS maps on the local region in 5182MZC alloy after isothermal aging at 400 °C for 12 h. Independent of the size and morphology, most dispersoids with bright contrast can be identified as $Al_6(Mn,Fe,Cr)$. In addition, coarse rhomboidal β-Mg_2Si phase with the size of a few hundred nanometers can also be observed.

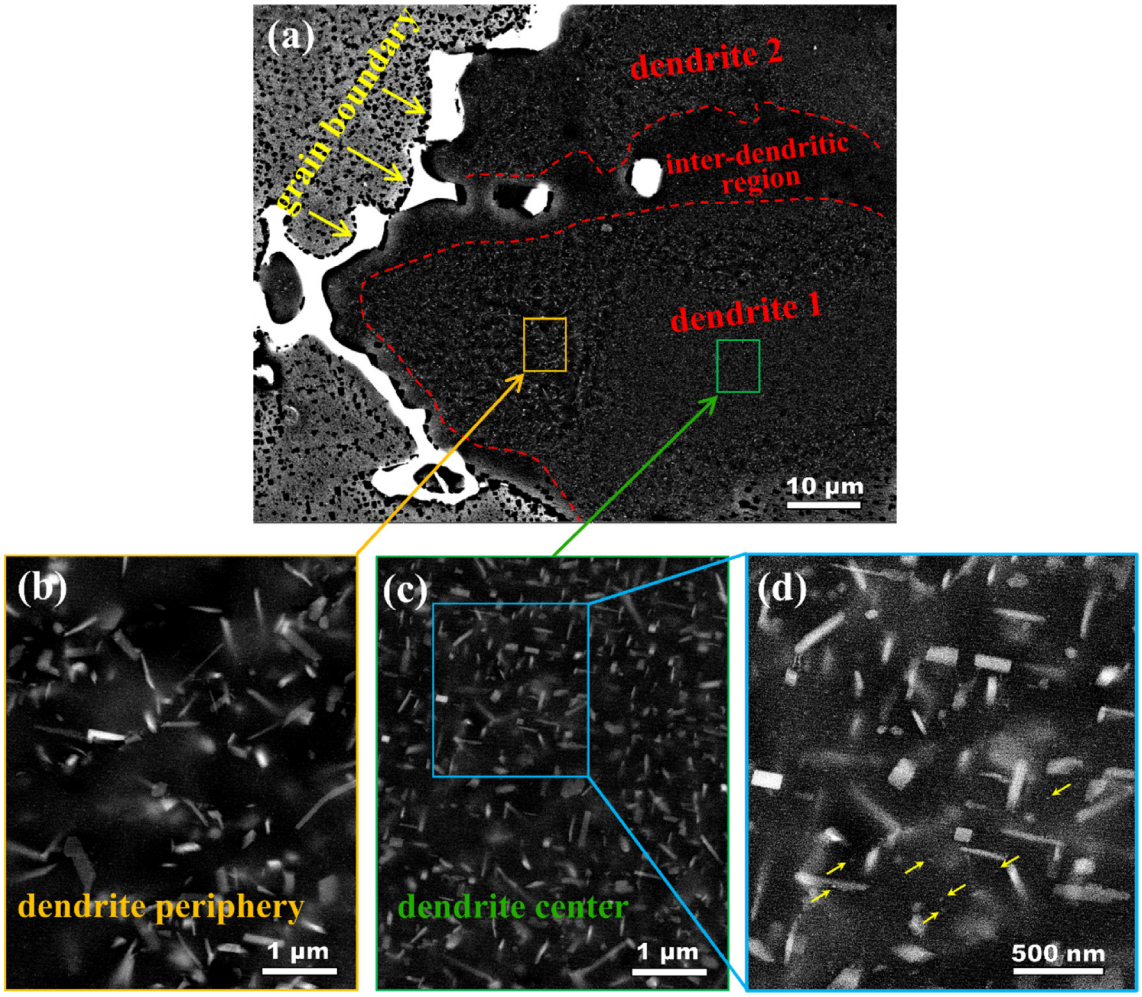

Fig. 9. SEM-BSE images of 5182MZC alloy after aging at 400 °C for 200 h. (a) Low-magnification image shows the overall distribution of dispersoids across the dendrite arms and inter-dendritic regions. Constituent phase formed during solidification generally distributes at grain boundaries and inter-dendritic regions. (b) and (c) are enlarged figures from dendrite periphery and center, respectively, showing the inhomogeneity of Mn-rich dispersoids. (d) High-magnification micrograph of dendrite center reveals the high density nano-sized dispersoids of both $Al_6(Mn,Fe,Cr)$ and Al_3Zr. Note small white spots in (c) are identified as fine Al_3Zr nanoparticles and some of them are marked by yellow arrows. (For interpretation of the references to color in this figure legend, the reader is referred to the web version of this article.)

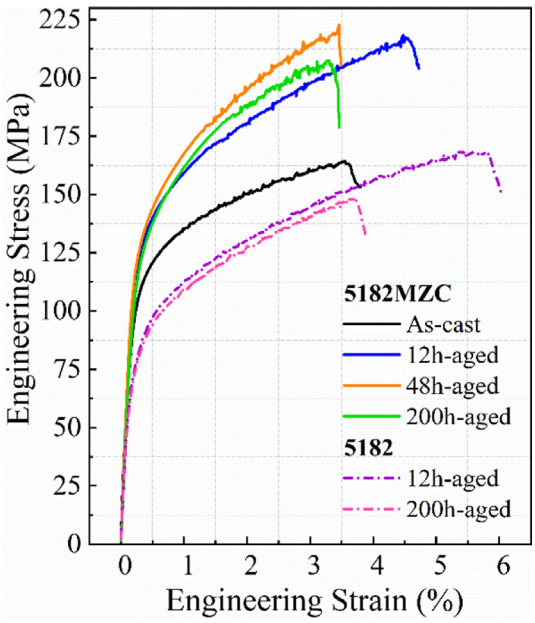

Fig. 10. Tensile stress-strain curves for 5182MZC and 5182 alloys after ramp-heating to 400 °C and then isothermal aging for various time. Note the tensile curve of 5182MZC at as-cast state is also displayed as a reference.

guished by their morphology and the distribution of low angle grain boundaries/subgrain boundaries. In this case, the unrecrystallized fraction is as high as 72 %, indicating a strong recrystallization resistance in the presence of dispersed Al_3Zr and Mn-rich dispersoids.

4. Discussion

4.1. Precipitation characteristics of dispersoids

In the present Al-Mg-Mn-Fe-Si-Zr-Cr alloy, high density of nano-sized dispersoids including both Al_3Zr and Mn-rich phases have been achieved after appropriate heat treatment regimes. Generally, the precipitation behavior of dispersoids is complicated in this multicomponent alloy system, which is related to the interactions between different phases/elements. As is found in Section 3, a fairly certain part of the precipitated Mn-rich dispersoids were identified as Al_6(Mn,Fe,Cr), while the fraction of α-Al(Mn,Fe)Si is lower. This observation is different from those in 3xxx [34], 6xxx [35] and some 5xxx series alloys (such as AA5052 [36]) although the presence of Si element can participate and accelerate the formation of Mn-bearing dispersoids. In fact, the high Mg:Si ratio in present 5182MZC alloy facilitates the formation of primary Mg_2Si particles during solidification (see Fig. 1c), thus reducing the Si content in Al matrix. In addition, during ramp heating procedure the precipitation of Mg_2Si happens at low temperature range and thus further scavenges residual Si solute atoms before the Mn decomposition, as seen in Fig. 3c. As a result, the precipitation of α-dispersoids is thermodynamically reduced, which is also in consistent with the findings in AA5083 alloy [20].

Based on the TEM results in Figs. 3 and 6, the precipitation sequence of dispersoids in 5182MZC alloy during aging can be clearly defined as formation of Mn-rich dispersoids including both α-dispersoids and Al_6(Mn,Fe,Cr) firstly, and then formation of Al_3Zr at higher temperature ranges. This discrepancy in precipitation kinetics mainly attributes to the higher diffusivity of Mn than that of Zr in fcc Al, considering both nucleation and growth of dispersoids are thermal-diffusion controlled processes [29]. However, it is worth of noting that the density of dispersed Al_3Zr is rather limited after ramp-heating to 550 °C. One important observation here is that the heterogeneous nucleation of Al_3Zr on pre-formed Mn-rich dispersoids (see Fig. 4 and section 3.2.2) reduces the supersaturation of Zr solute atoms in Al matrix and therefore reduce the driving force for homogeneous nucleation directly in the matrix. Besides, it may also be associated with dissolution of Mg_2Si phase in the range of 500–550 °C, thus giving rise to a re-increase of Si content in solid solution. Solute Si element was known to accelerate the coarsening rate of Al_3Zr by enhancing Zr diffusion [37,38]. In this case, coarsening of Al_3Zr will be accelerated as a result. In comparison, isothermal aging after ramp-heating to 400 °C is conducive to achieving a good combination of both nano-sized Al_6(Mn,Fe,Cr) and Al_3Zr, as shown in Fig. 6.

4.2. Effect of Cr-addition on Mn-rich dispersoids

Cr, as a typical dispersoid-forming element in Al, acts an important role in the precipitation of dispersoids in the present work. It was reported that several Cr-containing dispersoids, such as α-Al(Cr,Fe)Si and α'-AlCrSi, can precipitate during high temperature annealing (>520 °C) in Al-Si-Mg [39] and Al-Mg-Si [40] alloys. However, it is identified that during aging solute Cr has participated the precipitation of Mn-rich dispersoids (especially for Al_6(Mn,Fe,Cr)) in the present 5182MZC alloy, as shown in Figs. 3 and 8. Therefore, the addition of 0.2 wt% Cr indeed contributes to increase the volume fraction of Al_6(Mn,Fe,Cr) dispersoids. More importantly, the enrichment of peritectic Cr element in the dendritic center regions can provide enough driving force for the precipitation of Mn-rich dispersoids, although in these regions there is a depletion of Mn solute due to its opposite segregation mode during solidification. As a result, the global distribution of the Mn-rich dispersoids across dendrite arms is distinctly improved, and dense Al_6(Mn,Fe,Cr), instead of wide precipitate-free-zones, can be observed in the center of dendrites after aging (Fig. 9).

Similar to Mo [41], the partitioning of Cr into Mn-rich dispersoids was also reported to markedly influence the heat resistance of the dispersoids in Al alloys [30,42]. As seen in Section 3.3.2, the size of Mn-rich dispersoids is increased from 36.9 nm to 65.3 nm while the density of the dispersodis is still high after 200 h long time exposure at 400 °C, which shows better a heat resistance compared with our previous study of a Cr-free Al-Mn-Fe-Si-Zr alloy [29]. This should be associated with the fact that the diffusivity of Cr in fcc Al (3.2×10^{-21} m^2/s) is almost two orders of magnitude lower than that of Mn (6.4×10^{-19} m^2/s) at 400 °C

Table 2
Tensile yield strength (YS), ultimate strength (UTS) and elongation (EL) of studied alloys at different states in the present study.

Alloy	State	YS (MPa)	UTS (MPa)	EL (%)
5182	400 °C/12 h aged	90.8 ± 1.3	167.7 ± 5.4	5.4 ± 0.8
	400 °C/200 h aged	89.1 ± 1.5	150.2 ± 8.2	3.8 ± 0.6
5182MZ	As-cast	111.7 ± 7.6	165.0 ± 4.0	3.6 ± 0.9
	400 °C/12 h aged	134.6 ± 4.1	218.7 ± 16.2	4.2 ± 0.7
	400 °C/48 h aged	135.1 ± 10.1	223.1 ± 19.5	3.2 ± 1.0
	400 °C/200 h aged	133.5 ± 1.4	208.1 ± 14.6	2.9 ± 0.5

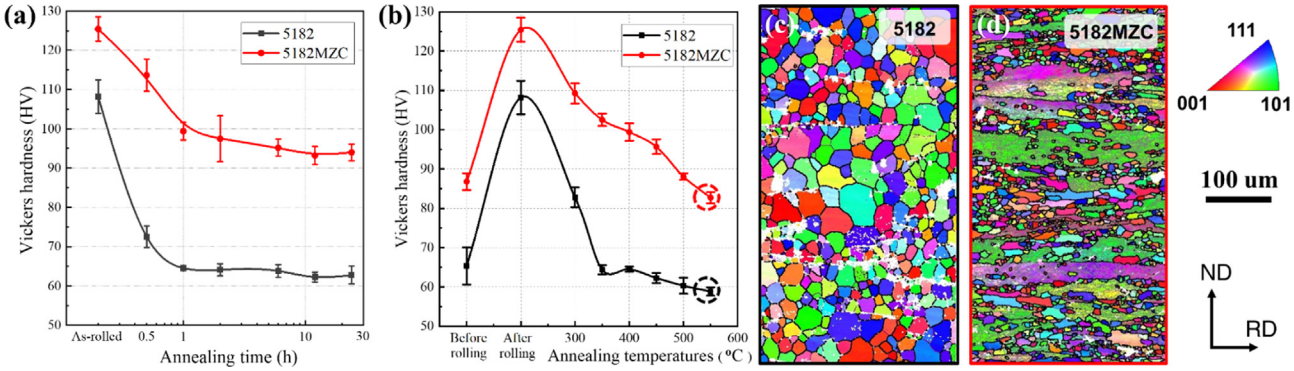

Fig. 11. Hardness evolution of 75 % cold-rolled 5182 and 5182MZC alloys: (a) during isothermal annealing at 400 °C until 24 h, (b) after annealing at different temperatures for 1 h. (c, d) EBSD-IPF maps of 5182 and 5182MZC alloys after annealing at 550 °C for 1 h, respectively, showing their grain structures. Note high angle grain boundaries (>15°) and low angle grain boundaries/subgrain boundaries (3–15°) are represented by black lines and grey lines, respectively. The unindexed areas in white color are coarse intermetallic phases distributed along grain boundaries as shown in Fig. 1c.

[29,43]. One characteristic evidence related to this mechanism is that in the dendrite center where there is a high Cr content, dense Al_6(Mn,Fe,Cr) particles with rather small size can be still observed after 200 h aging, as shown in Fig. 9a and c. Therefore, it is reasonable to expect that Cr can improve the thermal stability of Mn-rich dispersoids at 400 °C.

4.3. Dispersion-strengthening from dispersoids

The application of dispersion-strengthening in Al alloys is usually restricted by either low density or low volume fraction of dispersoids. In the present 5182MZC alloy, the precipitation of mainly two kinds of nano-sized phases, Mn-rich dispersoids and Al_3Zr, is proved to enhance the dispersion-hardening response, leading to age hardening like hardness curves during the applied heat treatments. The obtained hardness increments of 5182MZC at peak-aged state are 9.2 and 11.8 HV during ramp heating and isothermal aging, respectively. However, it should be mentioned that the precipitation of Mn-rich dispersoids also greatly decreases the Mn and Cr contents in Al matrix, thus reducing their solid solution strengthening at the same time. Taking this factor into consideration, the actual hardening contribution from dispersoids should be much higher than the observed hardness increment. It can be seen from Fig. 10 that a superior yield strength of 134.6 MPa is achieved in 5182MZC alloy after 12 h isothermal aging, which is 48.3 MPa (48 %) higher than that of the reference 5182 alloy. This improvement in yield strength is mainly ascribed to the high density and volume fraction of dispersoids across dendrite arms/-grains. In addition, these dispersoids exhibit high heat resistance at 400 °C. Usually, the dispersion hardening effect caused by Mn-rich dispersoids decreases quickly during exposure to this temperature [30] due to the coarsening of the dispersoids. In this work, the reduction of strengthening effect by Mn-rich dispersoids can be compensated by the continuous precipitation of nano Al_3Zr precipitates. As a result, no obvious change in yield strength can be detected after 200 h aging. Therefore, it demonstrates that 5182MZC owns a good thermal stability at 400 °C and shows the potential to be used for high temperature applications.

4.4. Effect of dispersoids on recrystallization

For as-rolled commercial 5182 alloy, a full recrystallization has been achieved after 1 h annealing at 350 °C, with a total hardness reduction of 44 HV, which completely levels off the work hardening (43 HV) arisen from 75 % cold rolling (Fig. 11b). This observation is similar to the results found in Al-5 Mg [44] and AA5050 [45] alloys. In contrast, a significantly retarded recrystallization is achieved in 5182MZC alloy, which should be mainly ascribe to the dense dispersoids formed before cold rolling. Both Al_3Zr and (Mn, Cr)-rich disperosids own high thermal stability due to the low diffusivities of Zr and Cr and thus can provide Zener pinning force on the migration of dislocations and (sub)grain boundaries during high temperature annealing. Herein, the Zener force (P_Z) can be described by the classical equation [19]:

$$P_Z = \frac{3f_v\gamma_{GB}}{2r}$$

where γ_{GB} is the specific grain boundary energy, f_v and r are the volume fraction and radius of dispersoids, respectively. For 5182MZC alloy, the synergistic additions of Mn, Zr and Cr, together with an optimized heat treatment (aging), results in a high volume fraction of small dispersoids (high f_v/r ratio), which is essentially required to achieve a higher Zener force. In addition, the homogeneous spatial distribution of dispersoids across the grains/dendrites (see section 3.3.2) in 5182MZC is also of great importance.

As a result, the recrystallization resistance of 5182MZC is obviously stronger than that of other commercial AA5xxx alloys which are only either Mn-containing [19,46] or Zr-containing [47,48].

Fig. 11d demonstrates a partially recrystallized microstructure of 5182MZC alloy However, upon annealing at 550 °C (~0.8Tm), coarsening of both types of dispersoids will become significant and the pinning effect will be reduced. As a result, the recrystallizaiton will start. After 1 h annealing, the hardness value of 83 HV is found to be lower than that of sample before rolling (87 HV). This reflects the loss in dispersion-strengthening effect due to the coarsening of dispersoids.

5. Conclusions

In this work, a new 5182MZC alloy was designed on the basis of AA5182 alloy with an increased Mn content to 1 wt% and micro-alloying of Zr and Cr. During ramp heating and 400 °C isothermal aging, the precipitation behavior of various dispersoids and their dispersion-hardening effect were systematically investigated. In addition, the effect of dispersoids on the recrystallization behavior of the cold-rolled alloys was also assessed. The major conclusions can be drawn as follow:

(1) High density of nano-sized particles including both Mn-rich dispersoids (α-Al(Mn,Fe)Si and Al_6(Mn,Fe,Cr) types) and Al_3-Zr are achieved in 5182MZC alloy upon aging. The precipitation kinetics of Mn-rich dispersoids is obviously faster than that of Al_3Zr, which can be attributed to the higher diffusivity of Mn than Zr in Al solid solution.

(2) It is found that coarse lath shaped Al_3Zr phase with $L1_2$ structure could nucleate on pre-formed Mn-rich dispersoids in 5182MZC alloy during ramp heating.
(3) A superior dispersion-strengthening effect with a yield strength of 135 MPa is obtained in 5182MZC alloy after 400 °C isothermal aging, which is 48 MPa (48 %) higher than that of the reference 5182 alloy. The modified alloy also shows a high thermal stability at 400 °C. Upon 200 h heating, the alloy keeps almost constant yield strength. This has been attributed to the continuous precipitation of Al_3Zr nanoparticles during 400 °C heating, which compensates the strength loss caused by the coarsening of Mn-reach dispersoids.
(4) The micro-addition of 0.2 wt% Cr significantly promotes the precipitation of dense and fine Mn-rich dispersoids in the dendritic center regions, thus improving their global distribution across dendrite arms. Moreover, the partitioning of Cr into the Mn-rich dispersoids slows down the coarsening kinetics because of the lower diffusivity of Cr than that of Mn.
(5) With a proper aging treatment before cold rolling, the as-rolled 5182MZC exhibits an outstanding softening resistance at elevated temperatures. With the presence of homogeneously distributed dense dispersoids, only partial recrystallization can be achieved in 5182 MZC after annealing at 550 °C for 1 h.

Data availability

The authors declare that data analyzed and shown in the paper is available from the corresponding authors on reasonable request.

CRediT authorship contribution statement

Shiwei Pan: Investigation, Data curation, Writing – original draft. **Zidong Wang:** Supervision, Funding acquisition. **Chunan Li:** Investigation, Writing – review & editing. **Di Wan:** Investigation, Writing – review & editing. **Xiaohua Chen:** Resources. **Kaixuan Chen:** Resources. **Yanjun Li:** Conceptualization, Supervision, Writing – review & editing, Funding acquisition.

Data availability

Data will be made available on request.

Declaration of Competing Interest

The authors declare that they have no known competing financial interests or personal relationships that could have appeared to influence the work reported in this paper.

Acknowledgment

The author SP would like to acknowledge the China Scholarship Council (“State Scholarship Fund”, No. 201906460095) for the scholarship granted to support this work. Dr. Yudong Cao is greatly acknowledged for TEM samples preparation.

References

[1] G. Yi, B. Sun, J.D. Poplawsky, Y. Zhu, M.L. Free, Investigation of pre-existing particles in Al 5083 alloys, J. Alloys Compd. 740 (2018) 461–469, https://doi.org/10.1016/j.jallcom.2017.12.329.
[2] R.E. Sanders, S.F. Baumann, H.C. Stumpf, Wrought Non-Heat-Treatable Aluminum Alloys, Treatise on Materials Science & Technology. Elsevier, 1989.
[3] Ø. Ryen, O. Nijs, E. Sjolander, B. Holmedal, H. Ekstro, E. Nes, Strengthening Mechanisms in Solid Solution Aluminum Alloys, Metall. Mater. Trans. A. 37A (2006) 1999–2006, https://doi.org/10.1007/s11661-006-0142-7.
[4] A.Y. Algendy, K. Liu, X.-G. Chen, Formation of intermetallic phases during solidification in Al-Mg-Mn 5xxx alloys with various Mg levels, MATEC Web Conf. 326 (2020) 02002, https://doi.org/10.1051/matecconf/202032602002.
[5] L. Zhao, H. Yan, J. Chen, W. Xia, B. Su, M. Song, Z. Li, X. Li, Y. Liao, High ductility and strong work-hardening behavior of Zn modified as-hot-rolled Al–Mg sheets, J. Alloys Compd. 854 (2021), https://doi.org/10.1016/j.jallcom.2020.157079 157079.
[6] G. Yi, Measuring and modeling the long-term sensitization behaviour of Al 5xxx alloys, The University of Utah, 2017.
[7] A.Y. Algendy, K. Liu, X.G. Chen, Evolution of dispersoids during multistep heat treatments and their effect on rolling performance in an Al-5% Mg-0.8% Mn alloy, Mater. Charact. 181 (2021), https://doi.org/10.1016/j.matchar.2021.111487 111487.
[8] Y.J. Li, L. Arnberg, Quantitative study on the precipitation behavior of dispersoids in DC-cast AA3003 alloy during heating and homogenization, Acta Mater. 51 (2003) 3415–3428, https://doi.org/10.1016/S1359-6454(03)00160-5.
[9] Y.J. Li, A.M.F. Muggerud, A. Olsen, T. Furu, Precipitation of partially coherent α-Al(Mn, Fe)Si dispersoids and their strengthening effect in AA 3003 alloy, Acta Mater. 60 (2012) 1004–1014, https://doi.org/10.1016/j.actamat.2011.11.003.
[10] J. Li, X. Yang, S. Xiang, Y. Zhang, J. Shi, Y. Qiu, R.E. Sanders, Effects of Sc and Zr addition on microstructure and mechanical properties of AA5182, Materials. 14 (2021) 4753, https://doi.org/10.3390/ma14164753.
[11] K. Huang, K. Zhang, K. Marthinsen, R.E. Logé, Controlling grain structure and texture in Al-Mn from the competition between precipitation and recrystallization, Acta Mater. 141 (2017) 360–373, https://doi.org/10.1016/j.actamat.2017.09.032.
[12] A.G. Mochugovskiy, A.V. Mikhaylovskaya, N.Y. Tabachkova, V.K. Portnoy, The mechanism of $L1_2$ phase precipitation, microstructure and tensile properties of Al-Mg-Er-Zr alloy, Mater. Sci. Eng. A. 744 (2019) 195–205, https://doi.org/10.1016/j.msea.2018.11.135.
[13] A.V. Mikhaylovskaya, V.K. Portnoy, A.G. Mochugovskiy, M.Y. Zadorozhnyy, N.Y. Tabachkova, I.S. Golovin, Effect of homogenisation treatment on precipitation, recrystallisation and properties of Al-3%Mg-TM alloys (TM = Mn, Cr, Zr), Mater. Des. 109 (2016) 197–208, https://doi.org/10.1016/j.matdes.2016.07.010.
[14] F. Bakare, L. Schieren, B. Rouxel, L. Jiang, T. Langan, A. Kupke, M. Weiss, T. Dorin, The impact of $L1_2$ dispersoids and strain rate on the Portevin-Le-Chatelier effect and mechanical properties of Al-Mg alloys, Mater. Sci. Eng. A. 811 (2021), https://doi.org/10.1016/j.msea.2021.141040 141040.
[15] J.D. Robson, O. Engler, C. Sigli, A. Deschamps, W.J. Poole, Advances in microstructural understanding of wrought aluminum alloys, Metall. Mater. Trans. A. 51 (2020) 4377–4389, https://doi.org/10.1007/s11661-020-05908-9.
[16] S. Pan, X. Chen, X. Zhou, Z. Wang, K. Chen, Y. Cao, F. Lu, S. Li, Micro-alloying effect of Er and Zr on microstructural evolution and yield strength of Al-3Cu (wt.%) binary alloys, Mater. Sci. Eng. A. 790 (2020), https://doi.org/10.1016/j.msea.2020.139391 139391.
[17] K.E. Knipling, D.C. Dunand, D.N. Seidman, Criteria for developing castable, creep-resistant aluminum-based alloys - A review, Zeitschrift Für Met. 97 (2006) 246–265.
[18] P.A. Rometsch, Y. Zhu, X. Wu, A. Huang, Review of high-strength aluminium alloys for additive manufacturing by laser powder bed fusion, Mater. Des. 219 (2022), https://doi.org/10.1016/j.matdes.2022.110779 110779.
[19] K. Huang, K. Marthinsen, Q. Zhao, R.E. Logé, The double-edge effect of second-phase particles on the recrystallization behaviour and associated mechanical properties of metallic materials, Prog. Mater. Sci. 92 (2018) 284–359, https://doi.org/10.1016/j.pmatsci.2017.10.004.
[20] O. Engler, S. Miller-Jupp, Control of second-phase particles in the Al-Mg-Mn alloy AA 5083, J. Alloys Compd. 689 (2016) 998–1010, https://doi.org/10.1016/j.jallcom.2016.08.070.
[21] O. Engler, K. Kuhnke, J. Hasenclever, Development of intermetallic particles during solidification and homogenization of two AA 5xxx series Al-Mg alloys with different Mg contents, J. Alloys Compd. 728 (2017) 669–681, https://doi.org/10.1016/j.jallcom.2017.09.060.
[22] Y.J. Li, W.Z. Zhang, K. Marthinsen, Precipitation crystallography of plate-shaped Al_6(Mn, Fe) dispersoids in AA5182 alloy, Acta Mater. 60 (2012) 5963–5974, https://doi.org/10.1016/j.actamat.2012.06.022.
[23] P. Ratchev, B. Verlinden, P. Van Houtte, Effect of preheat temperature on the orientation relationship of (Mn, Fe)A_l6 precipitates in an AA 5182 Aluminium-Magnesium alloy, Acta Metall. Mater. 43 (1995) 621–629, https://doi.org/10.1016/0956-7151(94)00261-F.
[24] P.A. Hollinshead, Effect of preheat treatment on ingot structure and recrystallisation of brass component of rolling texture in hot rolled AA 5182, Mater. Sci. Technol. 8 (1992) 56–62, https://doi.org/10.1179/026708392790169795.
[25] O. Engler, Z. Liu, K. Kuhnke, Impact of homogenization on particles in the Al-Mg-Mn alloy AA 5454-Experiment and simulation, J. Alloys Compd. 560 (2013) 111–122, https://doi.org/10.1016/j.jallcom.2013.01.163.
[26] S. Pan, Z. Wang, X. Chen, Y. Wang, K. Chen, Y. Zhu, Research progress in Zr-microalloying strengthened aluminum alloys, J. Mater. Eng. 50 (2022) 17–33, https://doi.org/10.11868/j.issn.1001-4381.2022.000087.
[27] A.V. Mikhaylovskaya, A.G. Mochugovskiy, V.S. Levchenko, N.Y. Tabachkova, W. Mufalo, V.K. Portnoy, Precipitation behavior of $L1_2$ Al_3Zr phase in Al-Mg-Zr

alloy, Mater. Charact. 139 (2018) 30–37, https://doi.org/10.1016/j.matchar.2018.02.030.
[28] A.G. Mochugovskiy, N.Y. Tabachkova, M.E. Ghayoumabadi, V.V. Cheverikin, A. V. Mikhaylovskaya, Joint effect of quasicrystalline icosahedral and $L1_2$-strucutred phases precipitation on the grain structure and mechanical properties of aluminum-based alloys, J. Mater. Sci. Technol. 87 (2021) 196–206, https://doi.org/10.1016/j.jmst.2021.01.055.
[29] S. Pan, F. Qian, C. Li, Z. Wang, Y. Li, Synergistic strengthening by nano-sized α-Al(Mn, Fe)Si and A_l3Zr dispersoids in a heat-resistant Al–Mn–Fe–Si–Zr alloy, Mater. Sci. Eng. A. 819 (2021), https://doi.org/10.1016/j.msea.2021.141460 141460.
[30] F. Qian, S. Jin, D. Wan, W. Li, X. Cheng, G. Sha, Y. Li, Synergistic effects of Cd, Si and Cr additions on precipitation strengthening and thermal stability of dispersoids in AA3003 alloy, Mater. Sci. Eng. A. 832 (2022), https://doi.org/10.1016/j.msea.2021.142422 142422.
[31] Astm-e21-09,, Standard Test Methods for Elevated Temperature Tension Tests of Metallic Materials, West Conshohocken, 2009.
[32] Y. Wang, C.M. Fang, L. Zhou, T. Hashimoto, X. Zhou, Q.M. Ramasse, Z. Fan, Mechanism for Zr poisoning of Al-Ti-B based grain refiners, Acta Mater. 164 (2019) 428–439, https://doi.org/10.1016/j.actamat.2018.10.056.
[33] A.M.F. Muggerud, J.C. Walmsley, R. Holmestad, Y. Li, Combining HAADF STEM tomography and electron diffraction for studies of α-Al(Fe, Mn)Si dispersoids in 3xxx aluminium alloys, Philos. Mag. 95 (2015) 744–758, https://doi.org/10.1080/14786435.2015.1006294.
[34] Q. Du, Y. Li, Effect modeling of Cr and Zn on microstructure evolution during homogenization heat treatment of AA3xxx alloys, Trans. Nonferrous Met. Soc. China. 24 (2014) 2145–2149, https://doi.org/10.1016/S1003-6326(14)63325-2.
[35] C.L. Liu, Q. Du, N.C. Parson, W.J. Poole, The interaction between Mn and Fe on the precipitation of Mn/Fe dispersoids in Al-Mg-Si-Mn-Fe alloys, Scr. Mater. 152 (2018) 59–63, https://doi.org/10.1016/j.scriptamat.2018.04.012.
[36] O. Engler, K. Kuhnke, K. Westphal, J. Hasenclever, Impact of chromium on the microchemistry evolution during solidification and homogenization of the Al-Mg alloy AA 5052, J. Alloys Compd. 744 (2018) 561–573, https://doi.org/10.1016/j.jallcom.2018.02.125.
[37] C. Booth-Morrison, Z. Mao, M. Diaz, D.C. Dunand, C. Wolverton, D.N. Seidman, Role of silicon in accelerating the nucleation of Al_3(Sc, Zr) precipitates in dilute Al-Sc-Zr alloys, Acta Mater. 60 (2012) 4740–4752, https://doi.org/10.1016/j.actamat.2012.05.036.
[38] A.R. Farkoosh, D.C. Dunand, D.N. Seidman, Effects of W and Si microadditions on microstructure and the strength of dilute precipitation-strengthened Al–Zr–Er alloys, Mater. Sci. Eng. A. 798 (2020), https://doi.org/10.1016/j.msea.2020.140159 140159.
[39] H. Zhan, B. Hu, Analyzing the microstructural evolution and hardening response of an Al-Si- Mg casting alloy with Cr addition, Mater. Charact. 142 (2018) 602–612, https://doi.org/10.1016/j.matchar.2018.06.026.
[40] L. Lodgaard, N. Ryum, Precipitation of chromium containing dispersoids in Al-Mg-Si alloys, Mater. Sci. Technol. 16 (2000) 599–604, https://doi.org/10.1179/026708300101508315.
[41] K. Liu, H. Ma, X.G. Chen, Enhanced elevated-temperature properties via Mo addition in Al-Mn-Mg 3004 alloy, J. Alloys Compd. 694 (2017) 354–365, https://doi.org/10.1016/j.jallcom.2016.10.005.
[42] Z. Li, J. Qin, B. Zhang, H. Nagaumi, Effect of cr addition on microstructure and mechanical properties at elevated temperature of almnmgsi alloys, Mater. Trans. 61 (2020) 2095–2100, https://doi.org/10.2320/matertrans.MT-M2020178.
[43] Y. Du, Y.A. Chang, B. Huang, W. Gong, Z. Jin, H. Xu, Z. Yuan, Y. Liu, Y. He, F.Y. Xie, Diffusion coefficients of some solutes in fcc and liquid Al: Critical evaluation and correlation, Mater. Sci. Eng. A. 363 (2003) 140–151, https://doi.org/10.1016/S0921-5093(03)00624-5.
[44] S.P. Wen, W. Wang, W.H. Zhao, X.L. Wu, K.Y. Gao, H. Huang, Z.R. Nie, Precipitation hardening and recrystallization behavior of Al-Mg-Er-Zr alloys, J. Alloys Compd. 687 (2016) 143–151, https://doi.org/10.1016/j.jallcom.2016.06.045.
[45] O. Engler, K. Knarbakk, Temper rolling to control texture and earing in aluminium alloy AA 5050A, J. Mater. Process. Tech. 288 (2021), https://doi.org/10.1016/j.jmatprotec.2020.116910 116910.
[46] N. Wang, J.E. Flatøy, Y.J. Li, K. Marthinsen, Evolution in microstructure and mechanical properties during back-annealing of AlMnFeSi alloy, Trans. Nonferrous Met. Soc. China. 22 (2012) 1878–1883, https://doi.org/10.1016/S1003-6326(11)61401-5.
[47] B. Morere, R. Shahani, C. Maurice, J. Driver, The influence of Al_3Zr dispersoids on the recrystallization of hot-deformed AA 7010 alloys, Metall. Mater. Trans. A. 32 (2001) 625–632, https://doi.org/10.1007/s11661-001-0079-9.
[48] Z. Guo, G. Zhao, X.G. Chen, Effects of two-step homogenization on precipitation behavior of Al_3Zr dispersoids and recrystallization resistance in 7150 aluminum alloy, Mater. Charact. 102 (2015) 122–130, https://doi.org/10.1016/j.matchar.2015.02.016.